**Astronomy
&
Astrophysics**

Fast MHD oscillations in prominence fine structures

A. J. Díaz[1], R. Oliver[1], R. Erdélyi[2], and J. L. Ballester[1]

[1] Departament de Física, Universitat de les Illes Balears, 07071 Palma de Mallorca, Spain
  e-mail: ramon.oliver@uib.es; dfsjlb0@uib.es
[2] Space & Atmosphere Research Center, Department of Applied Mathematics, University of Sheffield,
  Hicks Building, Hounsfield Road, Sheffield, S3 7RH, England, UK
  e-mail: Robertus@sheffield.ac.uk

Abstract. High-resolution observations suggest that quiescent solar prominences are made of small-scale fibrils stacked one after another in both the vertical and horizontal directions. These fibrils are interpreted as the cool, highermost part of much larger coronal loops which are rooted in the solar photosphere. On the other hand, there is some evidence showing that small amplitude oscillations in prominences can affect individual or groups of fibrils, which vibrate with their own periods. Using a simple magnetostatic model to represent the fibril structure of quiescent solar prominences, Joarder et al. (1997) investigated some oscillatory properties of the Alfvén and fast magnetohydrodynamic modes. In this paper, with a proper treatment of boundary conditions, we reexamine their configuration and explore more deeply the basic features (mainly frequency and spatial structure) of the fast mode. The main conclusion is that, for reasonable values of the fibril's width, perturbations extend far away from its axis and, therefore, a single oscillating fibril can excite oscillations in neighbouring ones.

Key words. Sun: oscillations – Sun: magnetic fields – Sun: corona – Sun: prominences

1. Introduction

Solar quiescent prominences are cool and dense objects which last for a long time and are embedded in the hot and rarefied solar corona. Many theoretical models have been put forward to explain the formation, support and disappearance of these intriguing objects, although no consensus about these issues has been reached yet (Webb et al. 1993). While some theoretical models consider prominences as an infinite slab of plasma having a small thickness, many observations of quiescent prominences show very fine structures in the body of the filament, suggesting that they are composed of small-scale threads. The existence of this internal structure in prominences was already suggested by Menzel & Evans (1953) and was clarified with the improvement of observational capabilities (Engvold 1976; Engvold et al. 1987). Although vertical filamentary structures can be seen in limb prominences (Dunn 1960), there is also evidence for the existence of horizontal fine structures within prominences (Schmieder & Mein 1989; Schmieder et al. 1991). For instance, Simon et al. (1986) studied the velocities in quiescent filaments in Hα and C IV. From the Hα observations they concluded that the filament is composed of many small-scale loops

anchored at many different footpoints that are not aligned along the filament axis. The observed vertical velocities and their changes due to perspective strongly suggest material falling down to the observed cool prominence, but whether this is material from the corona or over the top of a loop could not be distinguished. Demoulin et al. (1987) deduced statistical sizes of 10^3 km and 10^4 km for the thickness and length of the threads which form a filament. Engvold et al. (1987) studied a quiescent prominence seen in projection against the disk and, from the study of the prominence-corona interface, they deduced that the fine structure of the cool core of the prominence may consist of thin magnetic flux ropes oriented at an angle of $20°$ with the prominence long axis. Taking into account the observational evidence that solar prominences can be composed of small-scale loops, magnetostatic equilibrium models for prominence fibrils have been constructed by Ballester & Priest (1989), Degenhardt & Deinzer (1993) and Schmitt & Degenhardt (1996). These models represent a prominence fibril by means of a hot-cool loop modeled using the thin flux tube approximation. A different approach was used by Hood et al. (1992), Steele & Priest (1992) and Steele (1996), who modeled prominences as a vertical set of cold fibrils in the hotter corona, with ad hoc temperature profiles.

From the observational point of view, the existence of small amplitude, periodic velocity oscillations in quiescent solar prominences is a well-known phenomenon and many theoretical investigations have been undertaken to explain them. Periods of oscillation are classified as short ($T < 10$ min), intermediate (10 min $< T <$ 40 min) and long ($T > 40$ min) although this classification does not appear to reflect the origin of the prominence exciter (see Engvold 2001; Oliver & Ballester 2001 for a thorough review about prominence oscillations). In addition, it appears to be well established that small amplitude, periodic changes in solar prominences are of local nature, affecting only restricted prominence areas (Tsubaki & Takeuchi 1986; Tsubaki et al. 1987; Balthasar et al. 1988a; Balthasar et al. 1988b; Balthasar et al. 1993; Thompson & Schmieder 1991; Balthasar & Wiehr 1994). Two-dimensional, high-resolution observations (Yi et al. 1991; Yi & Engvold 1991) have even revealed that individual fibrils or groups of fibrils may oscillate independently with their own periods, which range between 3 and 20 min. Hence, one of the basic questions in prominence seismology that remains unanswered nowadays is whether periodic changes in prominences are always associated with their fibril structure or not.

The first theoretical investigation of periodic prominence perturbations taking into account the prominence fine structure was performed by Joarder et al. (1997), hereafter JNR97. In essence, the equilibrium is similar to that in Joarder & Roberts (1992) with the difference that the plasma slab has a limited height, so the configuration is reminiscent of a thin thread with finite width and length. Nevertheless, the fibril is infinitely deep since the equilibrium configuration is invariant in the y-direction. To further simplify the problem, the influence of plasma pressure was neglected (zero-β limit) and consequently the slow mode was absent. Thus, one is left with the Alfvén and fast modes in a plasma threaded by a transverse magnetic field. However, JNR97 did not properly incorporate the boundary conditions for the physical variables at one of the equilibrium interfaces and so their results for the fast mode are not completely correct. Moreover, these authors restricted their study to the oscillatory frequencies and did not take into account other properties that are also relevant.

A more suitable equilibrium model based on prominence fibrils was used by Rempel et al. (1999). It is built on the thin flux tube approximation in conjunction with the balance between heat conduction, radiative losses and heating. Nevertheless, the aim of this study was to investigate the stability properties of such prominence configuration under fast and slow mode perturbations and, consequently, the properties of stable modes were not analyzed in depth.

Our main goal in this paper is to properly solve, using both analytical and numerical tools, the problem of fast magnetohydrodynamic (MHD) oscillations of the fibril equilibrium configuration used by JNR97. To this end, our paper is organized as follows: In Sect. 2 the equilibrium model, the basic assumptions and the wave equations to be solved are described; Sect. 3 is devoted to describing the analytical solution of the fast magnetoacoustic wave equation, while Sect. 4 deals with the numerical solution; finally, in Sect. 5 we compare and discuss the analytical and numerical solutions and in Sect. 6 our conclusions are presented.

2. Basic equations

2.1. Equilibrium model

Following JNR97, we consider a single prominence fibril surrounded by the coronal medium (Fig. 1). This configuration consists of a straight flux tube of total length $2L$ made of a cold and dense part (the prominence fibril itself) with length $2W$ and density ρ_p and a hotter, coronal gas with density ρ_e occupying the reminder of the thin loop. This structure, whose thickness is $2b$, is embedded in the coronal environment, with density ρ_c. The loop is anchored in the photosphere, so its footpoints are subject to line-tying conditions. Finally, the plasma is permeated by a uniform magnetic field directed along the prominence fibril. Because gravity is neglected, all other physical variables (ρ, T and p) are also uniform in each of the three regions. In fact, in the present Cartesian configuration one cannot properly speak about a flux tube or a loop since the system is unlimited in the y-direction and so it is better described as a slab. Nevertheless, both terms will be used in the rest of the paper.

The parameter values used in this paper are similar to those considered by JNR97, where references to some relevant observational papers can be found. The thickness of prominence fibrils is $2b \simeq 200$–400 km and their length is $2W \simeq 20\,000$ km. The total length of magnetic field lines can be estimated as $2L \simeq 60\,000$–$200\,000$ km, so that $b/L \simeq 0.001$–0.007 and $W/L \simeq 0.1$–0.3. In addition, JNR97 use $\rho_e/\rho_c = 0.6$ and $\rho_p/\rho_c = 200$, so that the prominence material is 200 times more dense than the coronal one and the hot gas in the evacuated part of the loop is about half as dense as the coronal plasma. In our calculations we have also taken $\rho_c \simeq \rho_e$ and $\rho_p \simeq 1000\,\rho_c$, which corresponds to a still denser prominence compared to its surroundings (cf. Hvar Reference Atmosphere of Quiescent Prominences, Engvold et al. 1989).

2.2. Linear perturbation equations

Following JNR97, the equations governing the oscillatory modes are the linearized, ideal MHD equations for a zero-β plasma, where the subscript "0" denotes an equilibrium quantity,

$$\frac{\partial \rho}{\partial t} + \rho_0 \nabla \cdot \boldsymbol{v} = 0, \tag{1}$$

$$\rho_0 \frac{\partial \boldsymbol{v}}{\partial t} = \frac{1}{\mu}(\nabla \times \boldsymbol{B}) \times \boldsymbol{B}_0, \tag{2}$$
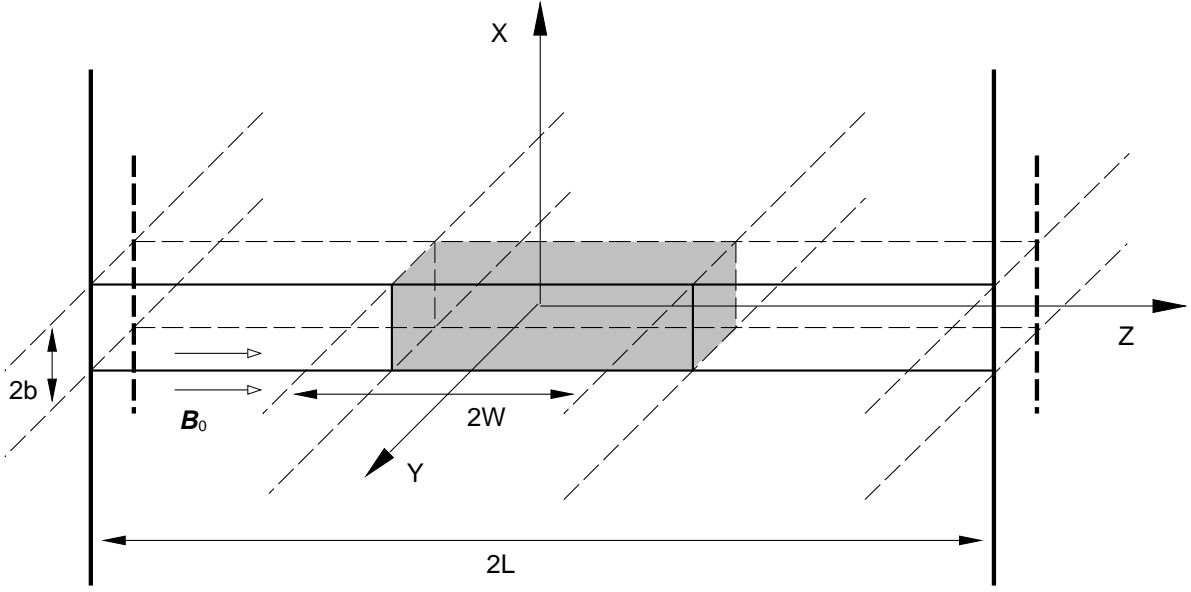
Fig. 1. Sketch of the equilibrium configuration used in this study. The grey zone represents the cold part of the loop, modeling the prominence fibril. The density in the fibril, $\rho_{\rm p}$, in the evacuated (coronal) part of the loop, $\rho_{\rm e}$, and in the coronal environment, $\rho_{\rm c}$, are all uniform. Moreover, the magnetic field is uniform and parallel to the z-axis and the whole configuration is invariant in the y-direction (After JNR97).

$$\frac{\partial \boldsymbol{B}}{\partial t} = \nabla \times (\boldsymbol{v} \times \boldsymbol{B}_0), \tag{3}$$

$$\nabla \cdot \boldsymbol{B} = 0. \tag{4}$$

The consequence of assuming zero plasma β is that the slow mode cannot propagate in this system and so, using the third component of the momentum equation, it turns out that $v_z = 0$. The other two components of Eq. (2) take the form

$$\rho_0 \frac{\partial v_x}{\partial t} = \frac{B_0}{\mu} \left(\frac{\partial b_x}{\partial z} - \frac{\partial b_z}{\partial x} \right), \tag{5}$$

$$\rho_0 \frac{\partial v_y}{\partial t} = \frac{B_0}{\mu} \frac{\partial b_y}{\partial z}, \tag{6}$$

where $\boldsymbol{b} = (b_x, b_y, b_z)$ is the perturbed magnetic field. Now, we write the components of the induction equation,

$$\frac{\partial b_x}{\partial t} = B_0 \frac{\partial v_x}{\partial z}, \qquad \frac{\partial b_y}{\partial t} = B_0 \frac{\partial v_y}{\partial z}, \qquad \frac{\partial b_z}{\partial t} = -B_0 \frac{\partial v_x}{\partial x}, \tag{7}$$

and next Fourier analyze all perturbed variables in time (i.e., each variable $\hat{a}(\boldsymbol{r}, t)$ is assumed to be of the form $\hat{a}(\boldsymbol{r}, t) = {\rm e}^{i\omega t} a(\boldsymbol{r})$, so $\partial/\partial t = i\omega$). Finally, after some simple algebra, we obtain the following partial differential equations for the velocity components v_x and v_y,

$$\frac{\partial^2 v_x}{\partial x^2} + \frac{\partial^2 v_x}{\partial z^2} + \frac{\omega^2}{v_{\rm A}^2} v_x = 0, \tag{8}$$

$$\frac{\partial^2 v_y}{\partial z^2} + \frac{\omega^2}{v_{\rm A}^2} v_y = 0, \tag{9}$$

with $v_{\rm A}$ the Alfvén speed. Equations (8) and (9) are two decoupled partial differential equations that govern the propagation of *fast magnetoacoustic waves* and

Alfvén waves, respectively. The spectrum and properties of Alfvén modes have already been discussed in JNR97, so we here concentrate on the investigation of fast modes.

3. Analytical solution

3.1. General method

We consider Eq. (8) and distinguish between two different zones: the flux tube (hereafter labelled "l") and the coronal environment (labelled "c"), with two different Alfvén speeds:

$$v_{\rm A} = \begin{cases} v_{\rm Ac}(z), & |x| > b, \\ v_{\rm Al}(z), & |x| < b. \end{cases} \tag{10}$$

The line-tying condition results in the boundary conditions

$$v_x = 0 \ \text{ at } \ z = \pm L. \tag{11}$$

Consider an ordinary differential operator $\mathcal{L}$, determined in the interval $[-L, L]$ by the differential expression

$$\frac{{\rm d}^2}{{\rm d}z^2} + \frac{\omega^2}{v_{{\rm A}j}^2(z)} \tag{12}$$

and the boundary conditions Eq. (11), where $j = {\rm c}, {\rm l}$, and c stands for external quantities and l for internal ones. It is straightforward to see that this operator is selfadjoint. According to the theory of selfadjoint ordinary regular differential operators, the eigenvalues of this operator constitute a monotonically decreasing countable set tending to $-\infty$. We write the nth eigenvalue as $-(\lambda_n^{(j)})^2$, where either $\lambda_n^{(j)} > 0$, or $\lambda_n^{(j)}$ is a purely imaginary number with

positive imaginary part, and $\lambda_n^{(j)} \to \infty$ as $n \to \infty$. The corresponding eigenfunction $h_n^{(j)}(z)$ satisfies the equation

$$\frac{d^2 h_n^{(j)}}{dz^2} + \frac{\omega^2}{v_{Aj}^2(z)} h_n^{(j)} = -(\lambda_n^{(j)})^2 h_n^{(j)}. \tag{13}$$

The set of eigenfunctions $\{h_n^{(j)}(z)\}$ constitute a complete system of functions (a basis) in $[-L, L]$, so that any well-behaved function $f(z)$ can be expanded into a generalized Fourier series

$$f(z) = \sum_{n=1}^{\infty} f_n^{(j)} h_n^{(j)}(z),$$

$$f_n^{(j)} = \left\langle f, h_n^{(j)} \right\rangle \equiv \int_{-L}^{L} f(z) h_n^{(j)}(z) \, dz, \tag{14}$$

where $\langle f, g \rangle$ indicates the scalar product of the functions f and g, and we have assumed that the basis $\{h_n^{(j)}(z)\}$ is orthonormal, i.e. $\|h_n^{(j)}\|^2 \equiv \langle h_n^{(j)}, h_n^{(j)} \rangle = 1$. Note that, by virtue of Eq. (13), the eigenvalues and eigenfunctions depend on ω.

Let us first find the solutions in the coronal region $(|x| > b)$. We expand v_x in series

$$v_x^{(c)}(x, z) = \sum_{n=1}^{\infty} u_n^{(c)}(x) h_n^{(c)}(z), \tag{15}$$

substitute this expansion into Eq. (8) and use Eq. (13). As a result we have an infinite set of equations for the coefficient-functions $u_n^{(c)}(x)$,

$$\frac{d^2 u_n^{(c)}}{dx^2} - (\lambda_n^{(c)})^2 u_n^{(c)} = 0. \tag{16}$$

The solutions to these equations, satisfying the condition $u_n^{(c)} \to 0$ as $|x| \to \infty$, are

$$u_n^{(c)} = \begin{cases} A_n^{(-)} \exp[\lambda_n^{(c)}(x+b)], & x < -b, \\ A_n^{(+)} \exp[-\lambda_n^{(c)}(x-b)], & x > b. \end{cases} \tag{17}$$

In what follows we consider only ω such that $(\lambda_1^{(c)})^2 > 0$, because otherwise the solution in the region $|x| > b$ does not tend to zero as $|x| \to \infty$. Since $\{(\lambda_n^{(c)})^2\}$ is a monotonically increasing set, $(\lambda_n^{(c)})^2 > 0$ for any n. Hence, the solution in the coronal part is

$$v_x^{(c)} = \begin{cases} \sum_{n=1}^{\infty} A_n^{(-)} \exp\left[\lambda_n^{(c)}(x+b)\right] h_n^{(c)}(z), & x < -b, \\ \sum_{n=1}^{\infty} A_n^{(+)} \exp\left[-\lambda_n^{(c)}(x-b)\right] h_n^{(c)}(z), & x > b. \end{cases} \tag{18}$$

Now we find the solution inside the tube $(|x| < b)$. We expand v_x in series

$$v_x^{(l)}(x, z) = \sum_{n=1}^{\infty} u_n^{(l)}(x) h_n^{(l)}(z), \tag{19}$$

substitute this expansion into Eq. (8) and use Eq. (13). As a result we have an infinite set of equations for the coefficient-functions $u_n^{(l)}(x)$,

$$\frac{d^2 u_n^{(l)}}{dx^2} - (\lambda_n^{(l)})^2 u_n^{(l)} = 0. \tag{20}$$

The solutions to these equations are

$$u_n^{(l)}(x) = B_n^{\cos} \cosh\left(\lambda_n^{(l)} x\right) + B_n^{\sin} \sinh\left(\lambda_n^{(l)} x\right). \tag{21}$$

Hence, the solution in the region $|x| < b$ is

$$v_x^{(l)} = \sum_{n=1}^{\infty} \left[B_n^{\cos} \cosh\left(\lambda_n^{(l)} x\right) + B_n^{\sin} \sinh\left(\lambda_n^{(l)} x\right) \right] h_n^{(l)}(z). \tag{22}$$

At the boundaries $|x| = b$, the normal component of the perturbed velocity and the magnetic field and the total magnetic pressure have to be continuous. In other words, our boundary conditions on those surfaces are

$$\boldsymbol{n} \cdot [\boldsymbol{v}] = 0, \quad \boldsymbol{n} \cdot [\boldsymbol{B}] = 0, \quad \left[p + \frac{B^2}{2\mu} \right] = 0, \tag{23}$$

where brackets represent $[A] \equiv A_2 - A_1$, the subscripts 1 and 2 indicating the values of the variable A on either side of the boundary.

The assumption of cold plasma leads to neglect the plasma pressure in front of the magnetic pressure, so the last condition of Eq. (23) follows from the second one. The conclusion from the development of Eqs. (1)–(4) and from Eq. (7) is that the second condition leads to continuity of $\partial v_x / \partial x$. Therefore, the conditions at $|x| = b$ are

$$v_x^{(c)} = v_x^{(l)}, \quad \frac{\partial v_x^{(c)}}{\partial x} = \frac{\partial v_x^{(l)}}{\partial x}. \tag{24}$$

Now, following Eq. (14), the functions $h_n^{(l)}(z)$ can be expanded into a "generalized Fourier series" in terms of the functions $h_n^{(c)}(z)$,

$$h_n^{(l)}(z) = \sum_{m=1}^{\infty} H_{nm} h_m^{(c)}(z). \tag{25}$$

The coefficients H_{nm} will play an important role in the following discussion. Using the completeness of our basis of eigenfunctions, the following expression for H_{nm} is obtained,

$$H_{nm} = \int_{-L}^{L} h_n^{(l)}(z) \, h_m^{(c)}(z). \tag{26}$$

After some algebraic manipulations (see Appendix A), the following expressions are obtained,

$$\sum_{m=1}^{\infty} H_{mn} B_m^{\sin} \left[\lambda_n^{(c)} \sinh\left(\lambda_m^{(l)} b\right) + \lambda_m^{(l)} \cosh\left(\lambda_m^{(l)} b\right) \right] = 0 \tag{27}$$

for sausage modes, and

$$\sum_{m=1}^{\infty} H_{mn} B_m^{\cos} \left[\lambda_n^{(c)} \cosh\left(\lambda_m^{(l)} b\right) + \lambda_m^{(l)} \sinh\left(\lambda_m^{(l)} b\right) \right] = 0 \tag{28}$$

for kink modes. By using this notation we are assuming the common terminology by which kink modes stand for even solutions in the direction across the fibril and sausage modes for the odd ones. These two kind of modes become separated because of the symmetry of the problem.

Equations (27) and (28) constitute two infinite systems of homogeneous algebraic equations for $B_m^{\sin}$ and $B_m^{\cos}$, respectively, with coefficients that depend on ω. For these systems to have non-trivial solutions, only particular values of ω are acceptable: the eigenfrequencies of the problem under consideration. Hence, the determinant of Eqs. (27) or (28) must be zero, which provides us with the dispersion relation from which ω can be computed. Since it is not possible to solve these infinite determinants, they are truncated by taking $B_n^r = 0$ ($r = \sin, \cos$) for $n > N$. Then, we obtain a generalized eigenvalue problem, with N a sufficiently large integer number for a finite matrix, and the eigenfrequencies can be determined from the condition that the determinant of the $N \times N$ matrix is zero, which results in a transcendental equation for ω.

After solving the dispersion relation to calculate the eigenfrequency ω, all other quantities can be calculated straightforward, except for the coefficients B_n^r. These ones must be obtained from the systems of equations in Eqs. (27) and (28), using the fact that for the eigenfrequencies the equations in these systems are not linearly independent, so all the coefficients B_n^r can be expressed in terms of B_1^r, which can be set to 1. Finally, the perturbed velocity can be obtained from Eqs. (15) and (19). The process of computing v_x is therefore quite cumbersome.

3.2. Application to fibril structure model

After having developed the previous theoretical frame we can turn to our model again. First of all, the Alfvén speed is v_{Ac} outside the fibril, whereas inside is defined as

$$v_{\mathrm{Al}}(z) = \begin{cases} v_{\mathrm{Ap}}, & |z| < W, \\ v_{\mathrm{Ae}}, & W < |z| < L, \end{cases} \tag{29}$$

where v_{Ac}, v_{Ap} and v_{Ae} are constant, and $v_{\mathrm{Ap}} < v_{\mathrm{Ae}}$. It is straightforward to find that

$$h_{2n-1}^{(\mathrm{c})}(z) = \frac{1}{L^{1/2}} \cos \frac{\pi(2n-1)z}{2L}, \tag{30}$$

$$h_{2n}^{(\mathrm{c})}(z) = \frac{1}{L^{1/2}} \sin \frac{\pi n z}{L},$$

$$\left(\lambda_{2n-1}^{(\mathrm{c})}\right)^2 = \frac{\pi^2(2n-1)^2}{4L^2} - \frac{\omega^2}{v_{\mathrm{Ac}}^2}, \tag{31}$$

$$\left(\lambda_{2n}^{(\mathrm{c})}\right)^2 = \frac{\pi^2 n^2}{L^2} - \frac{\omega^2}{v_{\mathrm{Ac}}^2},$$

where $n = 1, 2, \ldots$ The following quantities are also defined,

$$\kappa_{\mathrm{c}}^{\mathrm{od}} = \frac{\pi(2n-1)}{2L}, \quad \kappa_{\mathrm{c}}^{\mathrm{ev}} = \frac{\pi n}{L}. \tag{32}$$

According to the evanescent wave condition $(\lambda_1^{(\mathrm{c})})^2 > 0$, $\omega < \pi v_{\mathrm{Ac}}/(2L)$ (for even modes). This condition has been

derived under the assumption that $u_1^{(\mathrm{c})} \neq 0$, since no solutions can be found when this basis function is not included in the sum shown in Eq. (15). Furthermore, there are no solutions which show a decay in the x-direction for values of ω bigger than that one. We will comment on this point later.

Since one of the coefficients of the equation for $h_n^{(1)}(z)$ is discontinuous, the second derivative of $h_n^{(1)}(z)$ is discontinuous, while its first derivative and the function itself are continuous. However, at the boundaries $z = \pm W$ there is a different situation: the dot product of the equilibrium magnetic field and the normal is not zero, so the boundary conditions are more restrictive than Eqs. (23) (see Schmidt 1979; Goedbloed 1983),

$$[\boldsymbol{v}] = \boldsymbol{0}, \quad [\boldsymbol{B}] = \boldsymbol{0}, \quad [p] = 0. \tag{33}$$

These conditions imply the continuity of the functions $h_n^{(1)}$ and their derivatives at this boundary.

The solution to Eq. (13), satisfying the condition $h_n^{(1)}(\pm L) = 0$ is

$$h_n^{(1)}(z) = \begin{cases} C_- \sin[\kappa_{\mathrm{e}}(z + L)], & -L < z < -W, \\ D_{\cos} \cos(\kappa_{\mathrm{p}} z) \\ \quad + D_{\sin} \sin(\kappa_{\mathrm{p}} z), & -W < z < W, \\ C_+ \sin[\kappa_{\mathrm{e}}(z - L)], & W < z < L, \end{cases} \tag{34}$$

where

$$\kappa_{\mathrm{p}}^2 = \left(\lambda^{(1)}\right)^2 + \frac{\omega^2}{v_{\mathrm{Ap}}^2}, \quad \kappa_{\mathrm{e}}^2 = \left(\lambda^{(1)}\right)^2 + \frac{\omega^2}{v_{\mathrm{Ae}}^2}. \tag{35}$$

In these equations and in the following, the subscript n in the quantities $\kappa_{\mathrm{p}}, \kappa_{\mathrm{e}}, \kappa_{\mathrm{c}}, C_-, C_+, D_{\cos}, D_{\sin}$ and $\Lambda_{\mathrm{ev}}, \Lambda_{\mathrm{od}}$ (see below) has been dropped to simplify the notation.

At this point, the spatial dependence of v_x inside and outside the fibril is well characterized and so it is possible to discuss the differences between our solution and that in JNR97. Equations (18) and (22), with Eqs. (30) and (34) for $h_n^{(\mathrm{c})}(z)$ and $h_n^{(1)}(z)$, tell us that v_x is an infinite sum of basis functions with different wavelengths in the z-direction inside and outside the fibril. Because of the complex nature of this solution, imposing the boundary conditions (24) at the frontier between the two regions yields a dispersion relation which is the determinant of an infinite system of algebraic equations (Eqs. (27) and (28)). The situation looks much simpler in JNR97, whose Eqs. (16), (19) and (20) provide v_x inside and outside the loop using only one basis function in each region. The problem with JNR97's solution is that it cannot satisfy the boundary conditions at $|x| = b$ since the wavelength of outside and inside the loop are different along this boundary. For this reason, their condition (24) makes no sense.

In the parameter range of interest $\kappa_{\mathrm{p}}^2 > 0$ holds, while the sign of κ_{e}^2 can be arbitrary. Now it will be assumed that κ_{e} is either positive or purely imaginary with positive imaginary part. Nevertheless, in our model at least

the fundamental basis function has $\kappa_e < 0$ (and depending on the choice of parameters, this can be true for other harmonics too), so Eq. (34) should be written in terms of hyperbolic functions for this basis function (see Appendix B).

The continuity conditions at $z = \pm W$ lead to

$$C_- \sin[\kappa_e(L - W)] = D_{\cos} \cos(\kappa_p W)$$
$$-D_{\sin} \sin(\kappa_p W), \tag{36}$$

$$\kappa_e C_- \cos[\kappa_e(L - W)] = \kappa_p[D_{\cos} \sin(\kappa_p W)$$
$$+D_{\sin} \cos(\kappa_p W)], \tag{37}$$

$$-C_+ \sin[\kappa_e(L - W)] = D_{\cos} \cos(\kappa_p W)$$
$$+D_{\sin} \sin(\kappa_p W), \tag{38}$$

$$\kappa_e C_+ \cos[\kappa_e(L - W)] = \kappa_p[-D_{\cos} \sin(\kappa_p W)$$
$$+D_{\sin} \cos(\kappa_p W)]. \tag{39}$$

These expressions constitute a system of linear homogeneous equations with respect to C_-, C_+, $D_{\cos}$ and $D_{\sin}$, and has a non-trivial solution only if its determinant is zero, which gives

$$\kappa_p^2 \sin^2[\kappa_e(L - W)] \sin(2\kappa_p W)$$
$$-\kappa_p \kappa_e \sin[2\kappa_e(L - W)] \cos(2\kappa_p W) \tag{40}$$
$$-\kappa_e^2 \cos^2[\kappa_e(L - W)] \sin(2\kappa_p W) = 0.$$

There are two ways the previous equality can be satisfied,

$$\kappa_p \tan(\kappa_p W) = \kappa_e \cot[\kappa_e(L - W)] \tag{41}$$

or

$$\kappa_p \cot(\kappa_p W) = -\kappa_e \cot[\kappa_e(L - W)], \tag{42}$$

which are just Eqs. (22) and (23) in JNR97. It is straightforward to show that Eq. (42) corresponds to solutions to the system of Eqs. (36)–(39) with $D_{\sin} = 0$ and $C_+ = -C_-$, i.e. to even solutions, while Eq. (41) to solutions to the same system with $D_{\cos} = 0$ and $C_+ = C_-$, i.e. to odd solutions. According to the general theory of Sturm-Liouville problems, Eq. (41), considered as an equation for $(\lambda^{(1)})^2$, has an infinite set of solutions $\{(\lambda_{2n-1}^{(1)})^2\}$ such that $(\lambda_{2n-1}^{(1)})^2 \to \infty$ as $n \to \infty$. Equation (42), considered as an equation for $(\lambda^{(1)})^2$, also has an infinite set of solutions $\{(\lambda_{2n}^{(1)})^2\}$ such that $(\lambda_{2n}^{(1)})^2 \to \infty$ as $n \to \infty$. In addition, $(\lambda_{2n-1}^{(1)})^2 < (\lambda_{2n}^{(1)})^2 < (\lambda_{2n+1}^{(1)})^2$ for $n = 1, 2, \ldots$ Notice that in both cases the eigenvalues $\lambda_n^{(1)}$ depend on ω.

The even eigenfunctions are given by

$$h_{2n-1}^{(1)}(z) =$$
$$\Lambda_{ev} \begin{cases} \cos(\kappa_p W) \sin[\kappa_e(L + z)], & -L < z < -W, \\ \sin[\kappa_e(L - W)] \cos(\kappa_p z), & -W < z < W, \\ \cos(\kappa_p W) \sin[\kappa_e(L - z)], & W < z < L, \end{cases} \tag{43}$$

and the odd ones by

$$h_{2n}^{(1)}(z) =$$
$$\Lambda_{od} \begin{cases} -\sin(\kappa_p W) \sin[\kappa_e(L + z)], & -L < z < -W, \\ \sin[\kappa_e(L - W)] \sin(\kappa_p z), & -W < z < W, \\ \sin(\kappa_p W) \sin[\kappa_e(L - z)], & W < z < L. \end{cases} \tag{44}$$

The coefficients Λ_{ev} and Λ_{od} are determined by the normalization condition $\|h_{2n-1}^{(1)}\| = \|h_{2n}^{(1)}\| = 1$, i.e.

$$\int_{-L}^{L} [h_{2n-1}^{(1)}(z)]^2 \, dz = \int_{-L}^{L} [h_{2n}^{(1)}(z)]^2 \, dz = 1.$$

We can evaluate these coefficients by using Eqs. (43) and (44) to obtain the expressions

$$\Lambda_{ev}^{-2} = (L - W) \cos^2(\kappa_p W) + W \sin^2[\kappa_e(L - W)]$$
$$-\frac{1}{2\kappa_e} \cos^2(\kappa_p W) \sin[2\kappa_e(L - W)]$$
$$+\frac{1}{2\kappa_p} \sin^2[\kappa_e(L - W)] \sin(2\kappa_p W), \tag{45}$$

$$\Lambda_{od}^{-2} = (L - W) \sin^2(\kappa_p W) + W \sin^2[\kappa_e(L - W)]$$
$$-\frac{1}{2\kappa_e} \sin^2[\kappa_p W] \sin[2\kappa_e(L - W)]$$
$$-\frac{1}{2\kappa_p} \sin^2[\kappa_e(L - W)] \sin(2\kappa_p W). \tag{46}$$

The next step is to express the inner basis of functions in terms of the outer one. To achieve this we need to calculate the "Fourier coefficient" from Eq. (26). It is straightforward to check that even and odd parities are never mixed, i.e.

$$H_{2n,2m-1} = 0; \;\; m, n \in \mathcal{N}.$$

The other coefficients are given by

$$H_{2n,2m} = \Lambda_{od} L^{-\frac{1}{2}} \bigg\{ \sin[\kappa_e(L - W)]$$
$$\times \left(\frac{\sin[(\kappa_p - \kappa_c^{od})W]}{\kappa_p - \kappa_c^{od}} - \frac{\sin[(\kappa_p + \kappa_c^{od})W]}{\kappa_p + \kappa_c^{od}} \right)$$
$$+ \sin[\kappa_p W] \left(\frac{\sin[\kappa_e(L - W) - \kappa_c^{od}W]}{\kappa_e + \kappa_c^{od}} \right.$$
$$\left. - \frac{\sin[\kappa_e(L - W) + \kappa_c^{od}W]}{\kappa_e - \kappa_c^{od}} \right) \bigg\}, \tag{47}$$

$$H_{2n-1,2m-1} = \Lambda_{ev} L^{-\frac{1}{2}} \bigg\{ \sin[\kappa_e(L - W)]$$
$$\times \left(\frac{\sin[(\kappa_p - \kappa_c^{ev})W]}{\kappa_p - \kappa_c^{ev}} \right.$$
$$\left. + \frac{\sin[(\kappa_p + \kappa_c^{ev})W]}{\kappa_p + \kappa_c^{ev}} \right)$$
$$+ \cos[\kappa_p W] \left(-\frac{\cos[\kappa_e(L - W) - \kappa_c^{ev}W]}{\kappa_e + \kappa_c^{ev}} \right.$$
$$\left. - \frac{\cos[\kappa_e(L - W) + \kappa_c W]}{\kappa_e - \kappa_c^{ev}} \right) \bigg\}, \tag{48}$$

where the κ's are the ones defined by Eqs. (32) and (35), with the appropriate values of $\lambda_n^{(j)}$.

Now we have all the quantities that are needed in Eqs. (27) and (28). Notice that these two systems of equations are actually four once the even/odd symmetry in the z-direction is taken into account.

4. Numerical solution

Apart from the analytical method described in the previous section, a numerical approach has also been used to solve Eq. (8). There are a few reasons for using numerical techniques: first, if the cold plasma assumption is removed (such as must be done to better describe the real conditions in quiescent prominences), the mathematical problem changes to two coupled partial differential equations which are hard to solve analytically; second, the analytical solution involves large computational efforts when realistic (i.e. small) values of the fibril half-thickness, b, are considered. The advantage of having an analytical formalism to obtain fast mode frequencies is that the goodness of numerical values can be checked.

For these reasons, the numerical code described in Oliver et al. (1996) has been used. This program gives, among other information, the frequency and spatial structure of the fast and slow magnetoacoustic modes of any two-dimensional, y-invariant equilibrium with $B_y = 0$. Since we are concerned with solving Eq. (8), obtained under the $\beta = 0$ assumption, it is necessary to set the sound speed to zero to eliminate the slow mode.

Nevertheless, before applying the numerical code to the present problem it had to be modified so that the thin fibril and the much wider coronal environment can be adequately represented by a computational mesh with non-uniform spacing (see Appendix C for details). Previous versions of the code are not suitable for this task since they make use of a grid with two different but constant spacings in the x- and z-directions. Hence, to obtain a fine spatial representation of the velocity inside the fibril it would have been necessary to use an excessively small grid spacing, with the associated enormous computational cost.

Our use of the non-uniform grid consists essentially of taking a uniform mesh (although with different spacing in the x- and z-directions) covering the whole prominence fibril. The fibril is then surrounded by a coarser mesh which is in turn embedded in one or more even coarser grids that span the rest of the system. Therefore, the finite difference formulas for the derivatives of the velocity components are second order accurate in each of the regions (see Appendix C), but are only first order accurate at the interfaces between regions. Since the number of points in these interfaces is much smaller than the total number of points used, almost second order accuracy of eigensolutions is ensured.

Finally, we turn to the boundary conditions that must be imposed on v_x. Such as we mentioned before, this velocity component must vanish at $z = \pm L$ because of photospheric line-tying. On the other hand, v_x must also vanish as $|x| \to \infty$ and it is expected that solutions will decay exponentially in the x-direction. Hence, we place two horizontal boundaries sufficiently far from the thin loop (at $x = \pm H$, say) and impose $v_x = 0$ there. If these boundaries have been put far enough from the loop, the frequency and spatial structure of v_x remain unaltered when

H is increased. It turns out that it is necessary to set H some orders of magnitude larger than the thickness of the fibril in order to correctly reproduce the exponential decay in the x-direction (e.g. Fig. 6c).

5. Results

First of all, we mention the parameter values used in our calculations. Following JNR97, we set $W/L = 0.1$ for a fibril whose length is one tenth the total length of the thin loop (including both the cool and the evacuated parts). In addition, the following density ratios are considered, $\rho_e/\rho_c = 0.6$ and $\rho_p/\rho_c = 200$. These variables are useful because the equilibrium magnetic field is uniform and so the Alfvén speed in the hot and cool parts of the loop can be cast as $v_{Ae}^2 = \frac{\rho_c}{\rho_e} v_{Ac}^2$ and $v_{Ap}^2 = \frac{\rho_c}{\rho_p} v_{Ac}^2$. Now, all quantities can be non-dimensionalized against L and v_{Ac}, and Eq. (8) can be solved by analytical or numerical means. There is still a free parameter, namely b/L, whose value must be specified before these equations can be solved to find the eigenfrequencies and spatial properties of the modes.

Finally, it is worth commenting on the number of basis functions, N, to be used when Eqs. (27) or (28) are truncated. Tests have been done by using 8 and 10 basis functions and the difference in the frequency is of the order 0.01%. Consequently, frequencies have been computed using 8 basis functions (that is, only values up to $m = 8$ have been retained in Eqs. (27) and (28)). Regarding the eigenfunction, v_x, it is not well reproduced with such a small number of basis functions for realistic values of the fibril thickness ($b/L \simeq 0.001$–0.005) and many more basis functions are needed in order to capture well the spatial structure of the modes.

5.1. Dependence of fast mode frequency on the fibril thickness

We first study the dependence of the mode frequency on the half-thickness of the fibril, b. The analytical results for even and odd modes are plotted separately in Figs. 2a and b, which clearly show the presence of frequency cut-offs at $\omega_{cut} = \frac{\pi}{2} \frac{v_{Ac}}{L}$ and at $\omega_{cut} = \pi \frac{v_{Ac}}{L}$, respectively. These upper cut-offs were already discussed by JNR97 and they are important since, for $\omega > \omega_{cut}$, modes become leaky and decay in time by driving waves in the coronal medium. The occurrence of cutoffs is similar to that found for coronal slabs and loops (e.g. Edwin & Roberts 1982, 1983; Roberts et al. 1984), but there are some facts here that should be highlighted.

It must be emphasized that the difference between the analytical treatment in JNR97 and ours is that those authors just used one basis function for each mode, so their solution does not match properly at the boundary $b = L$ and can be considered a sort of first approximation to the correct solution. Hence, from the comparison between JNR97's Fig. 3 and our Fig. 2, it may seem that the proper treatment of this "jump" condition does not give rise to
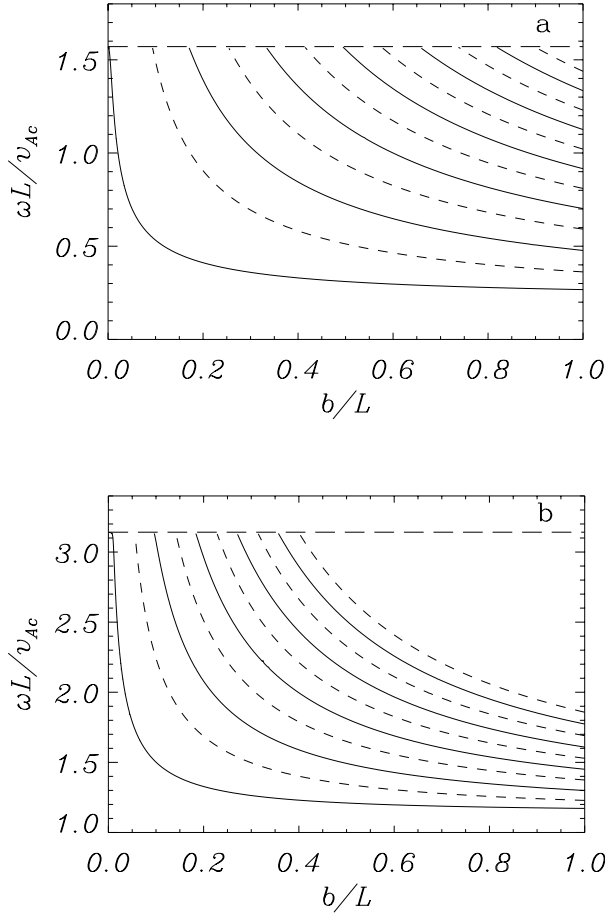
Fig. 2. Dimensionless frequency, $\omega L/v_{\rm Ac}$, versus half-thickness of the prominence fibril, b/L, for **a)** even modes and **b)** odd modes (only the 5 lower frequency odd modes for each symmetry are shown). These results correspond to $W/L = 0.1$, $\rho_{\rm e}/\rho_{\rm c} = 0.6$ and $\rho_{\rm p}/\rho_{\rm c} = 200$. The solid lines represent kink modes whether the dashed ones are sausage modes.

drastic modifications in the frequency of modes, but it will now be shown that this is only the case for unrealistic values of the fibril thickness and that for $2b \leq 500$ km, such as suggested by observations, the ω and spatial properties of fast modes are the wrong ones if conditions (23) at $|x| = b$ are not considered. We have replotted Fig. 2 using a logarithmic axis for the fibril half-thickness (see Fig. 3) and it is obvious that the even and odd fundamental modes do not show a frequency cut-off and that, instead, they display a maximum at their respective $\omega_{\rm cut}$, which they approach asymptotically as $b \to 0$. This result is in contradiction with that obtained by JNR97, since their fundamental even and odd modes reach their corresponding cut-off frequency for $b_{\rm cut}/L = 0.08$ and 0.04, and become evanescent for $b < b_{\rm cut}$.

It has been said before that there is no solution for $\omega L/v_{\rm Ac} > \pi/2$ (even modes). In this situation the fundamental basis function becomes leaky and, because the summatory in Eq. (22) always includes this first basis function, no solution holds the requirement that $|u| \to 0$ exponentially as $|x| \to \infty$. That is the reason why all
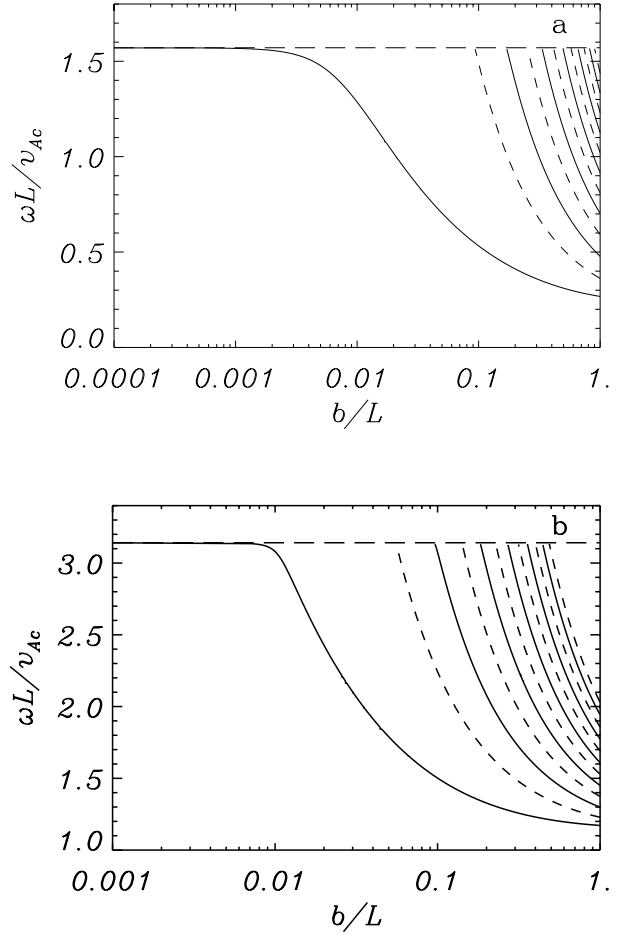
Fig. 3. Plot of the data in Fig. 2 using a logarithmic axis for b/L. Notice that fundamental even and odd modes do not have a frequency cut-off, but exist for very small values of the fibril thickness.

harmonics in Fig. 2 have the same cut-off frequency. Odd modes display a similar behaviour, but taking into account that the cut-off frequency is $\omega L/v_{\rm Ac} = \pi$.

5.2. Exploring the parameter space

We next investigate the effect of modifying the parameters $\rho_{\rm p}/\rho_{\rm c}$, $\rho_{\rm e}/\rho_{\rm c}$ and W/L with respect to the values considered so far. Some simulations have been performed with other possible combinations of these parameters since, in real prominences, different fibrils are probably characterized by different density and/or length. Our approach is to concentrate on the frequency of modes and to compare the resulting ω vs. b/L diagrams with Fig. 2.

Varying the quantity $\rho_{\rm e}/\rho_{\rm c}$ does not give rise to important changes in ω, specially because one does not expect the density in the coronal environment and in the evacuated part of the fibril to be much different from one another. Calculations have been carried out with $\rho_{\rm e}/\rho_{\rm c} = 0.3$ and $\rho_{\rm e}/\rho_{\rm c} = 1$, but the differences are very small (sometimes under our working precision).

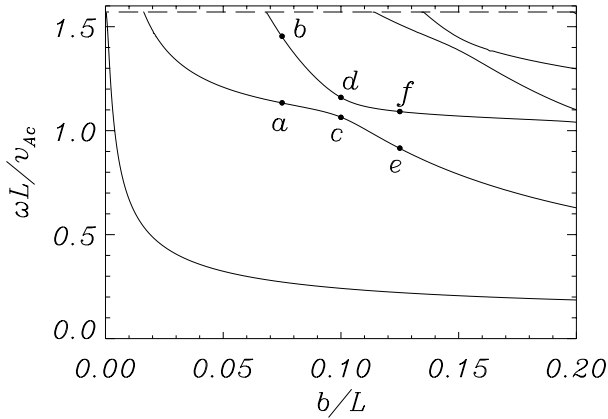The effects of modifying the other two parameters are more important and, for example, by increasing the ratio

Fig. 4. Variation of frequency with the fibril half-thickness for kink even modes ($W/L = 0.1$, $\rho_e/\rho_c = 1$ and $\rho_p/\rho_c = 1000$). A range of b/L smaller than that used in Figs. 2 and 3 has been selected to better show the behaviour for realistic values of this parameter. Dots are used to mark solutions for which the spatial profile of v_x is plotted in Fig. 5.

of prominence to coronal density from 200 to 1000 (quite a reasonable value), Fig. 2 changes to Fig. 4. It can be appreciated that, for a fixed fibril thickness, the number of normal modes supported by the fibril increases when ρ_p/ρ_c is increased (something similar happens with the parameter W/L). Therefore, for realistic values of $b/L \leq 0.01$, higher harmonics could also be excited in a prominence fibril.

Another noticeable effect in Fig. 4 is *mode coupling* between fast modes, which arises from their different spatial structure. Let us concentrate on the first and second kink even harmonics for $b/L = 0.075$ (points a and b in Fig. 4). Their corresponding eigenfunctions, shown in Figs. 5a and b, have two extrema in the x-direction and two extrema in the z-direction, respectively. During the coupling (points c and d in Fig. 4, $b/L = 0.1$) the two modes start to interchange their spatial structure (cf. Figs. 5c and d) and the extrema do not lie parallel to either the x- or z-axis. Finally, after the coupling (points e and f in Fig. 4, $b/L = 0.125$) the first harmonic displays two extrema in the x-direction, whereas the second harmonic has two extrema in the z-direction (Figs. 5e and f) and the structure interchange is finished. It is clear that this coupling is only possible because of the summation of different basis functions in Eqs. (15) and (19), which is forced by the fact that solutions must be continuous at the interfaces $|x| = b$. Obviously, the fundamental mode does not couple to higher harmonics because its spatial shape, with only one maximum, does not allow it to interact with other modes.

5.3. Spatial structure of eigenfunctions

We next concentrate on the shape of eigenfunctions. First of all, because of the sum in Eqs. (15) and (19), the obtained solutions are not separable functions in x and z (that is, $v_x(x, z) \neq f_1(x) \cdot f_2(z)$). This point has become

clear with the contour plots in Fig. 5, specially with panels c and d.

It was mentioned above that the fundamental kink even and odd modes are those suitable for driving oscillations in prominence fibrils, for which b/L is probably smaller than 0.01 (cf. Figs. 3 and 4). Thus, we start with the first of these modes and represent its spatial structure by means of cuts along the x- and z-directions. Figure 6a, which corresponds to a very thick fibril ($b/L = 0.1$), shows that the velocity amplitude quickly decays across the fibril ($x/L > 0.1$) and that it becomes almost zero at a distance about ten times the fibril half-thickness. Along the loop axis (Fig. 6b), v_x also decreases from its maximum value at the fibril centre. However, for a realistic, thin fibril there is a noticeable amplitude far away from the dense part (Fig. 6c) and it is necessary to move a distance $x \approx 10^3 - 10^4 \, b$ from the fibril for perturbations to vanish. Therefore, the excitation of this kind of modes in a prominence fibril can also excite perturbations in neighbouring threads and so it is expected that fibrils do not oscillate individually but in groups.

Regarding the kink odd fundamental mode, its spatial structure is such that v_x does not achieve its maximum amplitude at the fibril centre, but somewhere along the thin loop (see Fig. 7). In fact, for the values of b/L considered here, the velocity maximum occurs in the evacuated part of the loop rather than inside the cool region and the amplitude in the fibril decreases as the loop thickness is decreased. Thus, because of their small velocity inside fibrils, kink odd modes may be difficult to detect observationally.

Finally, it is worth mentioning what happens when other harmonics approach the cut-off frequency, a situation that can be studied with the numerical code. Just below ω_{cut} the velocity only vanishes at long distances from the fibril in the x-direction (similarly to the fundamental even kink mode, cf. Fig. 6c) and, as ω_{cut} is exceeded, the mode becomes a free wave and it does not satisfy the boundary conditions $v_x = 0$ as $x \to \pm\infty$.

5.4. Oscillatory period

We finally concentrate on the period of oscillation for various parameter values and compare them with observational data (see Table 1). Although the equilibrium configuration used lacks some of the properties of a real fibril, like its three-dimensional structure or the pressure gradient force, a comparison can be made. First of all, the parameters in JNR97 have been taken and, by comparing with their Table I, it turns out that periods are not too different when the MHD boundary conditions at the loop-corona interface are included. The reason for this behaviour is that the modes in JNR97 essentially correspond to the dominant terms in Eqs. (15) and (19) and so provide a good approximation to the mode frequency.

Signatures of periods in the 5–15 min range (such as the ones in Table 1) have been abundantly reported in
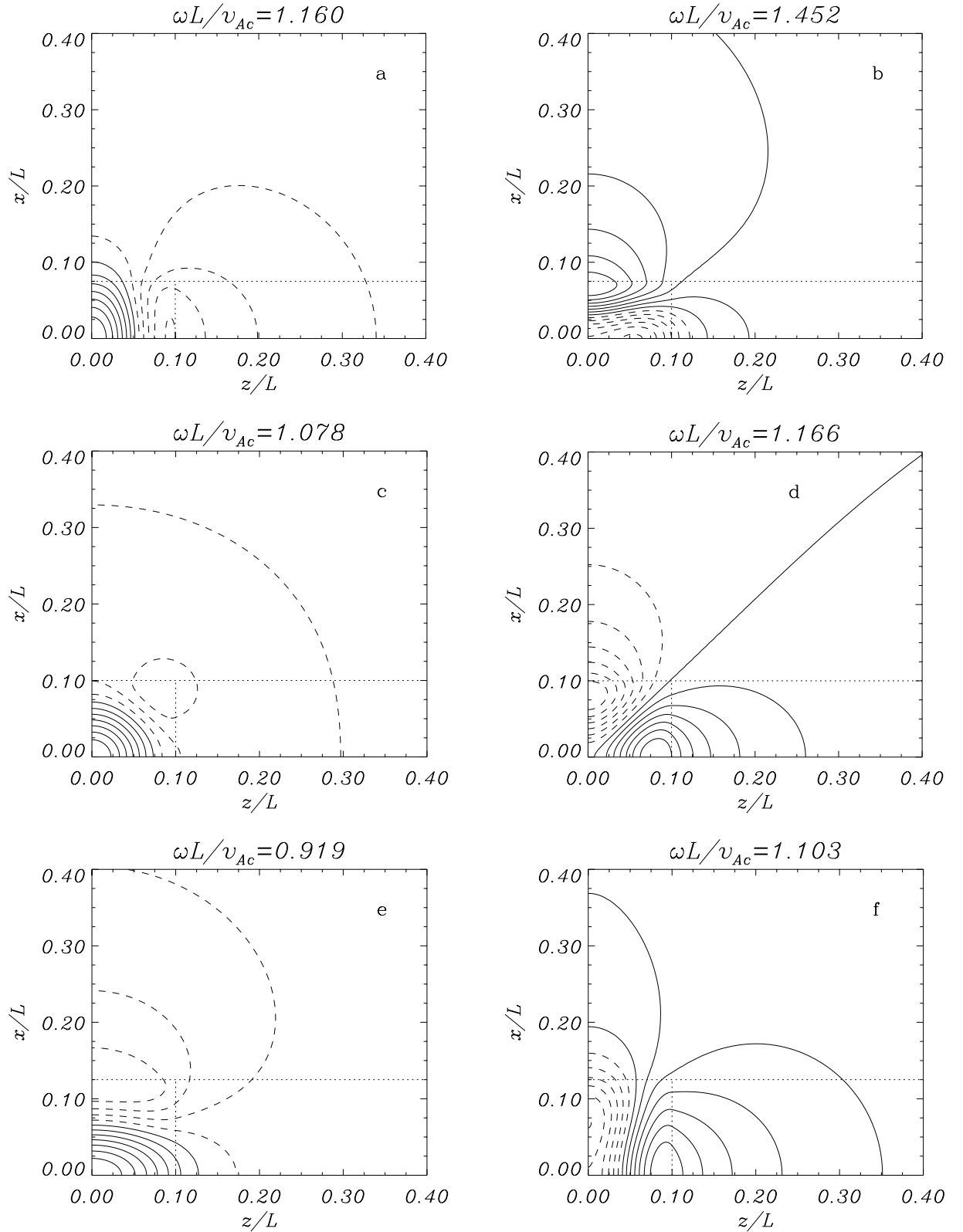
Fig. 5. Contour plots of v_x at the dots marked in Fig. 4, showing the change in shape of eigenfunctions as the first and second harmonics (kink even symmetry) couple together. These modes correspond to $W/L = 0.1$, $\rho_p/\rho_c = 1000$ and $\rho_e/\rho_c = 1$. The dimensionless fibril half-thickness is **a)** and **b)** $b/L = 0.075$, **c)** and **d)** $b/L = 0.1$, and **e)** and **f)** $b/L = 0.125$. Solid and dashed lines represent, respectively, positive and negative contour values, while the thick, solid line corresponds to zero v_x. The boundaries between the dense and evacuated part of the loop and the coronal medium have been plotted using dotted lines.
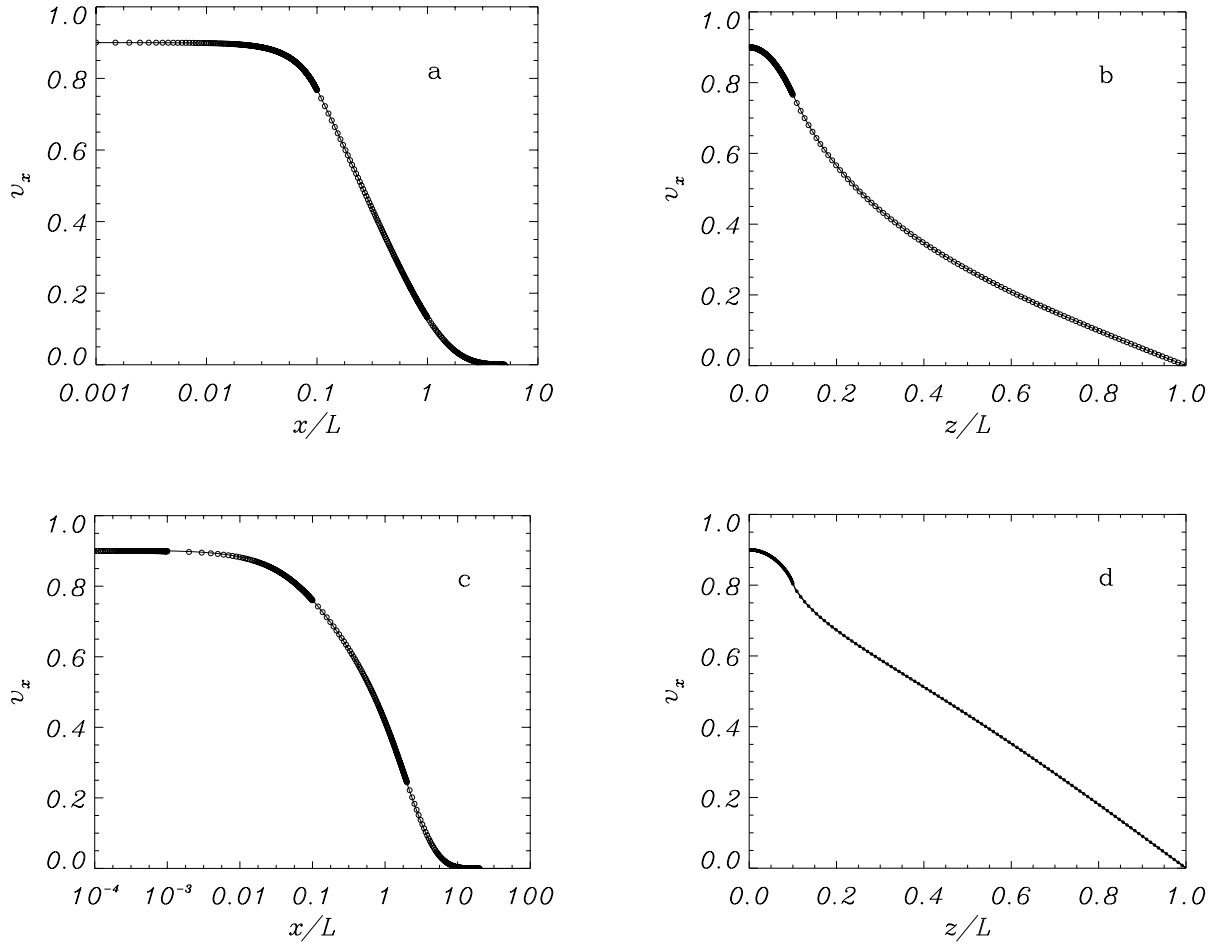
Fig. 6. The fundamental kink even mode has a single maximum located at $x = z = 0$. The spatial structure of this mode is here displayed for two different values of the fibril thickness through cuts **a)** and **c)** in the direction $z = 0$ (i.e. across the centre of the fibril), and **b)** and **d)** in the direction $x = 0$ (i.e. along the axis of the fibril). **a)** and **b)** v_x for a very thick fibril ($b/L = 0.1$), shown to illustrate the good agreement between the analytical and numerical solutions (solid lines and empty circles, respectively). **c)** and **d)** Analytical and numerical solutions (solid lines and empty circles) for a typical value of fibril thickness, $b/L = 0.001$. The number of basis functions kept to obtain the analytical solution is $N = 70$. Other parameter values used to obtain the two eigensolutions are $W/L = 0.1$, $\rho_{\rm p}/\rho_{\rm c} = 1000$ and $\rho_{\rm e}/\rho_{\rm c} = 1$. The use of various grids of different but uniform mesh sizes to properly capture the spatial structure of these modes is clearly appreciated in the four panels.

Table 1. Period of fast modes in a prominence fibril with $\rho_{\rm e}/\rho_{\rm c} = 0.6$, $\rho_{\rm p}/\rho_{\rm c} = 200$ and $W/L = 0.1$. The magnetic field strength and coronal density have been taken as $B_0 = 5$ G and $\rho_{\rm c} = 8.37 \times 10^{-13}$ kg/m^3, so the Alfvén speed is $v_{\rm Ac} = 488$ km s^{-1}.

Fast Mode	Type of solution	$L = 10^5$ km		$L = 3 \times 10^4$ km	
		$b = 100$ km	$b = 200$ km	$b = 100$ km	$b = 200$ km
Fundamental	numerical	13.70 min	13.79 min	4.83 min	5.77 min
kink even	analytical	13.70 min	13.80 min	4.79 min	5.81 min
Fundamental	numerical	6.84 min	6.84 min	2.47 min	3.15 min
kink odd	analytical	6.84 min	6.84 min	2.45 min	3.15 min

the literature, e.g. the 8–9 min and 14–16 min oscillations observed by Yi et al. (1991) and Yi & Engvold (1991). Obviously, this does not mean that waves detected by these authors are actually fast modes and until better models are considered and better experimental information becomes available it will be difficult to make a true comparison between theoretical and observational results.

6. Conclusions

Analytical and numerical techniques have been used in this paper to investigate the features of fast modes propagating in a thin, cool prominence fibril. Very accurate analytical solutions can be obtained with only a few basis functions for modes with simple spatial structure in thick
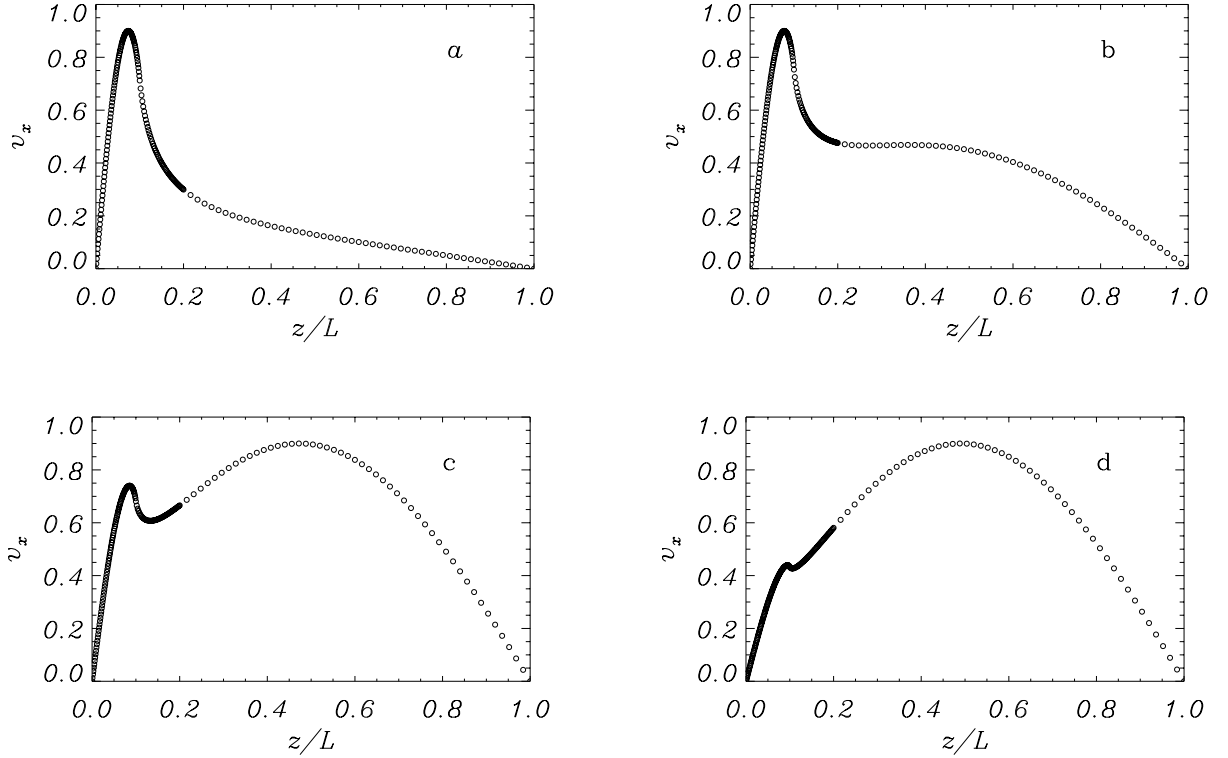
Fig. 7. Cuts of the velocity of the fundamental kink odd mode along the loop axis, $x = 0$, for $W/L = 0.1$, $\rho_{\mathrm{p}}/\rho_{\mathrm{c}} = 1000$, $\rho_{\mathrm{e}}/\rho_{\mathrm{c}} = 1$ and **a)** $b/L = 0.005$ ($\omega L/v_{A\mathrm{c}} = 2.063$), **b)** $b/L = 0.002$ ($\omega L/v_{A\mathrm{c}} = 3.036$), **c)** $b/L = 0.0015$ ($\omega L/v_{A\mathrm{c}} = 3.127$), and **d)** $b/L = 0.001$ ($\omega L/v_{A\mathrm{c}} = 3.140$). The four solutions have been computed numerically using a mesh of non-uniformly spaced points The mode also expands in the x-direction when b/L is raised (not shown in plots).

fibrils, but many more harmonics are needed for thin fibrils and/or higher harmonics (i.e. modes with more oscillations in the x- and/or z-direction), with the subsequent increase in the computational time required. In addition, obtaining v_x in thin fibrils by means of the analytical procedure is rather cumbersome and so the numerical code has been used for this task, although comparisons have been done (see for example Fig. 6) and the agreement is excellent. Besides, this code can be used to study other symmetries and to take into account the influence of slow modes when the plasma pressure is not neglected.

Two are the main conclusions that can be extracted from our results. First, prominence fibrils can only support a few modes of oscillation, those with smaller frequency, since high harmonics cannot be trapped inside the thin loop. Starting from a thick fibril, fast modes increase their frequency as the fibril thickness is reduced and, as soon as they exceed the cut-off frequency corresponding to kink and sausage modes, they become oscillatory. This is not the case, however, with the fundamental even and odd kink modes, whose ω tends asymptotically to ω_{cut} but never reaches this value. Second, it has been shown that the spatial structure of the fundamental even and odd kink modes is such that the velocity amplitude outside the fibril takes large values over long distances, the reason being that their frequency is so close to ω_{cut} that they are little confined to the prominence.

A consequence of the above results is that if fast modes were excited in the kind of fibril considered, most of the energy would be pumped out into the corona. Modes are not very well trapped by the fibril structure and, although the density of the coronal environment is very small compared to that of the dense material, the external region is much larger than the fibril and its total energy content can be comparable to the energy contained in the fibril. Therefore, this physical effect can give rise to damping of perturbations by means of energy leakage between fibrils. In addition, from the current view of prominences as made of a large number of thin fibrils packed together, it seems that fibrils would actually oscillate in groups rather than individually and that if a single fibril is disturbed it will excite perturbations in its neighbours, which may help to explain how prominence oscillations are damped in time. An important corollary is that the study of the collective modes of a multi-fibril prominence model is needed to better understand the oscillatory properties of these objects. Note that the above conclusion about fibrils oscillating in groups rather than individually is not in contradiction with the observations by Yi et al. (1991) and Yi & Engvold (1991) since the spatial resolution in their data is ≥ 1 arcsec.

There are many extensions that can be made on the present work. Nevertheless, the analytical solution developed here is no longer useful, except for the case of

cylindrical symmetry with no angular dependence and maybe for a slab with other density profiles. Further work will be done to use other features of the numerical code, like its ability to include slow modes by retaining the plasma pressure force.

Appendix A: Deduction of the dispersion relations

In this appendix the intermediate steps to obtain the dispersion relations are presented. Using Eqs. (17), (22) and (25), and imposing Eq. (24), we obtain

$$A_n^{(-)} = \sum_{m=1}^{\infty} H_{mn} \left[B_m^{\cos} \cosh\left(\lambda_m^{(1)} b\right) - B_m^{\sin} \sinh\left(\lambda_m^{(1)} b\right) \right], \text{(A.1)}$$

$$\lambda_n^{(c)} A_n^{(-)} = -\sum_{m=1}^{\infty} H_{mn} \lambda_m^{(1)} \left[B_m^{\cos} \sinh\left(\lambda_m^{(1)} b\right) - B_m^{\sin} \cosh\left(\lambda_m^{(1)} b\right) \right], \text{(A.2)}$$

$$A_n^{(+)} = \sum_{m=1}^{\infty} H_{mn} \left[B_m^{\cos} \cosh\left(\lambda_m^{(1)} b\right) + B_m^{\sin} \sinh\left(\lambda_m^{(1)} b\right) \right], \text{(A.3)}$$

$$\lambda_n^{(c)} A_n^{(+)} = -\sum_{m=1}^{\infty} H_{mn} \lambda_m^{(1)} \left[B_m^{\cos} \sinh\left(\lambda_m^{(1)} b\right) + B_m^{\sin} \cosh\left(\lambda_m^{(1)} b\right) \right]. \text{(A.4)}$$

Eliminating $A_n^{(-)}$ and $A_n^{(+)}$ from these equations, we obtain

$$\sum_{m=1}^{\infty} H_{mn} \left\{ B_m^{\cos} \left[\lambda_n^{(c)} \cosh\left(\lambda_m^{(1)} b\right) + \lambda_m^{(1)} \sinh\left(\lambda_m^{(1)} b\right) \right] \right.$$
$$\left. - B_m^{\sin} \left[\lambda_n^{(c)} \sinh\left(\lambda_m^{(1)} b\right) + \lambda_m^{(1)} \cosh\left(\lambda_m^{(1)} b\right) \right] \right\} = 0, \text{(A.5)}$$

$$\sum_{m=1}^{\infty} H_{mn} \left\{ B_m^{\cos} \left[\lambda_n^{(c)} \cosh\left(\lambda_m^{(1)} b\right) + \lambda_m^{(1)} \sinh\left(\lambda_m^{(1)} b\right) \right] \right.$$
$$\left. + B_m^{\sin} \left[\lambda_n^{(c)} \sinh\left(\lambda_m^{(1)} b\right) + \lambda_m^{(1)} \cosh\left(\lambda_m^{(1)} b\right) \right] \right\} = 0. \text{(A.6)}$$

We can further simplify this system of equations considering sausage ($B_m^{\cos} = 0$, odd modes about $x = 0$) and kink ($B_m^{\sin} = 0$, even modes about $x = 0$) oscillations separately. Notice that this could have been done in Eq. (22) by separating the two symmetries in the x-direction. We then obtain Eqs. (27) and (28) for sausage and kink modes simply by subtracting or adding Eqs. (A.5) and (A.6).

Appendix B: Special coefficients

It has been mentioned in Sect. 3 that $\kappa_e < 0$ holds for the first basis function $h_1^{(1)}$. For this function Eqs. (43), (44) are not valid, and must be replaced by

$$h_1^{(1)}(z) =$$
$$\Lambda_{ev}^* \begin{cases} \cos(\kappa_p W) \sinh[\kappa_e(L+z)], & -L < z < -W, \\ \sinh[\kappa_e(L-W)] \cos(\kappa_p z), & -W < z < W, \\ \cos(\kappa_p W) \sinh[\kappa_e(L-z)], & W < z < L, \end{cases}$$
$$\text{(B.1)}$$

and

$$h_1^{(1)}(z) =$$
$$\Lambda_{od}^* \begin{cases} -\sin(\kappa_p W) \sinh[\kappa_e(L+z)], & -L < z < -W, \\ \sinh[\kappa_e(L-W)] \sin(\kappa_p z), & -W < z < W, \\ \sin(\kappa_p W) \sinh[\kappa_e(L-z)], & W < z < L, \end{cases}$$
$$\text{(B.2)}$$

with

$$(\Lambda_{ev}^*)^{-2} = (L-W)\cos^2(\kappa_p W)$$
$$- W \sinh^2[\kappa_e(L-W)]$$
$$- \frac{1}{2\kappa_e} \cos^2(\kappa_p W) \sinh[2\kappa_e(L-W)]$$
$$- \frac{1}{2\kappa_p} \sinh^2[\kappa_e(L-W)] \sin(2\kappa_p W), \text{(B.3)}$$

$$(\Lambda_{od}^*)^{-2} = (L-W)\sin^2(\kappa_p W)$$
$$- W \sinh^2[\kappa_e(L-W)]$$
$$- \frac{1}{2\kappa_e} \sin^2(\kappa_p W) \sinh[2\kappa_e(L-W)]$$
$$+ \frac{1}{2\kappa_p} \sinh^2[\kappa_e(L-W)] \sin(2\kappa_p W). \text{(B.4)}$$

In addition, some coefficients in Eqs. (47) and (48) are also different,

$$H_{1,2m-1} = \Lambda_{od}^* L^{-\frac{1}{2}} \left\{ \sin[\kappa_e(L-W)] \right.$$
$$\times \left(\frac{\sin[(\kappa_p - \kappa_c^{ev})W]}{\kappa_p - \kappa_c^{ev}} + \frac{\sin[(\kappa_p + \kappa_c^{ev})W]}{\kappa_p + \kappa_c^{ev}} \right)$$
$$+ 2\frac{\cos(\kappa_p W)}{\kappa_e^2 + \kappa_c^{ev\,2}} (\kappa_e \cosh[\kappa_e(L-W)] \cos(\kappa_c^{ev} W)$$
$$\left. - \kappa_c^{ev} \sinh[\kappa_e(L-W)] \sin(\kappa_c^{ev} W)) \right\}, \text{(B.5)}$$

$$H_{2,2m} = \Lambda_{ev}^* L^{-\frac{1}{2}} \left\{ \sin[\kappa_e(L-W)] \right.$$
$$\times \left(\frac{\sin[(\kappa_p - \kappa_c^{od})W]}{\kappa_p - \kappa_c^{od}} - \frac{\sin[(\kappa_p + \kappa_c^{od})W]}{\kappa_p + \kappa_c^{od}} \right)$$
$$+ 2\frac{\sin(\kappa_p W)}{\kappa_e^2 + \kappa_c^{ev\,2}} (\kappa_e \cosh[\kappa_e(L-W)] \sin(\kappa_c^{ev} W)$$
$$\left. + \kappa_c^{ev} \sinh[\kappa_e(L-W)] \cos(\kappa_c^{ev} W)) \right\}. \text{(B.6)}$$

Equations (27) and (28) must be modified and, taking into account the above formulas, the dispersion relations for kink and sausage modes become

$$H_{1n}B_1^{\cos}\left[\lambda_n^{(c)}\cos\left(\lambda_1^{(1)}b\right) - \lambda_1^{(1)}\sin\left(\lambda_1^{(1)}b\right)\right] + \sum_{m=2}^{\infty} H_{mn}$$

$$\times B_m^{\cos}\left[\lambda_n^{(c)}\cosh\left(\lambda_m^{(1)}b\right) + \lambda_m^{(1)}\sinh\left(\lambda_m^{(1)}b\right)\right] = 0, \quad \text{(B.7)}$$

$$H_{1n}B_1^{\sin}\left[\lambda_n^{(c)}\sin\left(\lambda_1^{(1)}b\right) + \lambda_1^{(1)}\cos\left(\lambda_1^{(1)}b\right)\right] + \sum_{m=2}^{\infty} H_{mn}$$

$$\times B_m^{\sin}\left[\lambda_n^{(c)}\sinh\left(\lambda_m^{(1)}b\right) + \lambda_m^{(1)}\cosh\left(\lambda_m^{(1)}b\right)\right] = 0. \quad \text{(B.8)}$$

There is also another important remark: for other sets of parameters, other basis functions reach their critical frequency and then $\kappa_e < 0$ holds for them too. This has to be taken into account in Eqs. (B.7) and (B.8), which would have more terms in the sum similar to the first one.

The rest of the work has been done by numerical computations. First of all we need to solve Eqs. (42) and (41) numerically to obtain the set of eigenvalues. Then we can calculate the $\kappa's$ and the H_{nm} from Eqs. (B.5) and (B.6). Finally one is able to write down the determinant coming from Eqs. (B.8) and (B.7) and solve it to find out the characteristic frequencies of our model.

Appendix C: Finite-difference discretization of first and second order derivatives

Let us consider a two-dimensional mesh of points (ψ_i, χ_j) (following Oliver et al. 1996 we use the names ψ and χ for the variables in the plane perpendicular to the y-direction. In the present case, $\psi = z$ and $\chi = x$.) We define the grid spacings in the two directions as,

$$h_i = \psi_i - \psi_{i-1}, \qquad i = 2, 3, \ldots, N_\psi, \qquad \text{(C.1)}$$

$$g_j = \chi_j - \chi_{j-1}, \qquad j = 2, 3, \ldots, N_\chi, \qquad \text{(C.2)}$$

with N_ψ and N_χ the number of grid points in the ψ- and χ-directions. Next, consider a function $f(\psi, \chi)$ whose derivatives are to be approximated by finite difference formulas at a point (ψ_i, χ_j). We now expand the function f in Taylor series around this point to calculate its value at the eight mesh points around (ψ_i, χ_j) and obtain expressions of the form

$$f_{i+1,j} = f_{i,j} + h_{i+1}\frac{\partial f}{\partial\psi} + \frac{1}{2}h_{i+1}^2\frac{\partial^2 f}{\partial\psi^2}$$

$$+ \frac{1}{6}h_{i+1}^3\frac{\partial^3 f}{\partial\psi^3} + O\left(h_{i+1}^4\right), \qquad \text{(C.3)}$$

$$f_{i+1,j-1} = f_{i,j} + h_{i+1}\frac{\partial f}{\partial\psi} - g_j\frac{\partial f}{\partial\chi}$$

$$+ \frac{1}{2}h_{i+1}^2\frac{\partial^2 f}{\partial\psi^2} - h_{i+1}g_j\frac{\partial^2 f}{\partial\psi\partial\chi} + \frac{1}{2}g_j^2\frac{\partial^2 f}{\partial\chi^2}$$

$$+ \frac{1}{6}h_{i+1}^3\frac{\partial^3 f}{\partial\psi^3} - \frac{1}{2}h_{i+1}^2 g_j\frac{\partial^3 f}{\partial\psi^2\partial\chi}$$

$$+ \frac{1}{2}h_{i+1}g_j^2\frac{\partial^3 f}{\partial\psi\partial\chi^2} - \frac{1}{6}g_j^3\frac{\partial^3 f}{\partial\chi^3}$$

$$+ O\left(\max\left\{h_{i+1}^4, h_{i+1}^3 g_j, h_{i+1}^2 g_j^2, h_{i+1}g_j^3, g_j^4\right\}\right), \qquad \text{(C.4)}$$

where $f_{i,j} = f(\psi_i, \chi_j)$, $f_{i+1,j} = f(\psi_{i+1}, \chi_j)$, etc., and all partial derivatives are evaluated at the point (ψ_i, χ_j).

Now, approximate formulas for the partial derivatives can be determined by combining some or all of the above series expansions to eliminate unwanted partial derivatives. Then we have

$$\frac{\partial f}{\partial\psi} = \frac{1}{h_i + h_{i+1}}\left[p_i f_{i+1,j} + (q_i - p_i)f_{i,j}\right.$$

$$\left. - q_i f_{i-1,j}\right] + O(h_i h_{i+1}), \qquad \text{(C.5)}$$

where $p_i = h_i/h_{i+1} \equiv q_i^{-1}$. Notice that this expression, which is second order accurate in the mesh size, reduces to the well-known formula for equally spaced points after setting $h_i = h_{i+1} = h$.

Next, second-order derivatives are approximated by

$$\frac{\partial^2 f}{\partial\psi^2} = \frac{2}{h_{i+1}(h_i + h_{i+1})}f_{i+1,j} - \frac{2}{h_i h_{i+1}}f_{i,j}$$

$$+ \frac{2}{h_i(h_i + h_{i+1})}f_{i-1,j} + O\left(\frac{h_{i+1}^2 - h_i^2}{h_i + h_{i+1}}\right). \qquad \text{(C.6)}$$

This expression is first order accurate in h, but it becomes second order accurate for uniform spacing ($h_i = h_{i+1}$). There are other finite-difference formulas to compute this derivative using other combinations of $f_{i,j}$, $f_{i+1,j}$, etc., but none of them achieves second order accuracy.

Finally, the second order, cross derivative is also needed,

$$\frac{\partial^2 f}{\partial\psi\partial\chi} = \frac{\alpha_1}{h_{i+1}g_{j+1}}\left(f_{i+1,j+1} + f_{i,j} - f_{i,j+1} - f_{i+1,j}\right)$$

$$+ \frac{\alpha_2}{h_i g_{j+1}}\left(f_{i-1,j} + f_{i,j+1} - f_{i-1,j+1} - f_{i,j}\right)$$

$$+ \frac{\alpha_3}{h_i g_j}\left(f_{i,j} + f_{i-1,j-1} - f_{i-1,j} - f_{i,j-1}\right)$$

$$+ \frac{\alpha_4}{h_{i+1}g_j}\left(f_{i+1,j} + f_{i,j-1} - f_{i,j} - f_{i+1,j-1}\right). \text{(C.7)}$$

In order to get second order accuracy, the quantities α_1, α_2, α_3 and α_4 must satisfy the following conditions *at each point* (ψ_i, χ_j)

$$\alpha_2 = \frac{1}{s_j + 1} - \alpha_1, \qquad \text{(C.8)}$$

$$\alpha_3 = \frac{1}{p_i + 1} - \alpha_2, \qquad \text{(C.9)}$$

$$\alpha_4 = \frac{1}{q_i + 1} - \alpha_1, \qquad \text{(C.10)}$$

where $s_j = g_{j+1}/g_j$ and α_1 is a free parameter here taken equal to 0.25. This choice is not arbitrary, but arises from the fact that a possible set of values for a uniform mesh is $\alpha_1 = \alpha_2 = \alpha_3 = \alpha_4 = 0.25$.

So we are left with finite difference expressions for the first and second order derivatives of a function with respect to ψ and χ (the last ones are not given here and are similar to Eqs. (C.5) and (C.6)). This function can be either the normal or parallel velocity component (respectively v_x and v_z in the present configuration). Upon substituting the approximations for derivatives into the linearized MHD equations, one gets an algebraic eigenvalue system which is solved using the procedure described in Oliver et al. (1996).

References

Ballester, J. L., & Priest, E. R. 1989, A&A, 225, 213

Balthasar, H., & Wiehr, E. 1994, A&A, 204, 286

Balthasar, H., Wiehr, E., Schleicher, H., & Wöhl, H. 1993, A&A, 277, 635

Balthasar, H., Stellmacher, G., & Wiehr, E. 1988, A&A, 286, 639

Balthasar, H., Wiehr, E., & Stellmacher, G. 1988, in Dynamics and Structure of Solar Prominences, ed. J. L. Ballester, & E. R. Priest (Universitat de les Illes Balears, Spain), 63

Degenhardt, U., & Deinzer, W. 1993, A&A, 278, 288

Demoulin, P., Raadu, M., Malherbe, J. M., & Schmieder, B. 1987, A&A, 183, 142

Dunn, R. B. 1960, Ph.D. Thesis, Harvard University

Edwin, P. M., & Roberts, B. R. 1982, Sol. Phys., 76, 239

Edwin, P. M., & Roberts, B. R. 1983, Sol. Phys., 88, 179

Engvold, O. 1976, Sol. Phys., 49, 283

Engvold, O. 2001, in INTAS Workshop on MHD Waves in Astrophysical Plasmas, ed. J. L. Ballester, & B. Roberts (Universitat de les Illes Balears, Spain), in press

Engvold, O., Kjeldseth-Moe, O., Bartoe, J. D. F., & Brueckner, G. 1987, in Proc. of the 21st ESLAB Symp., ESA SP-275, 21

Engvold, O., Hirayama, T., Leroy, J. L., Priest, E. R., & Tandberg-Hanssen, E. 1989, in Dynamics of Quiescent Prominences, ed. V. Ruždjak, & E. Tandberg-Hanssen (Springer-Verlag), IAU Colloq., 117, 296

Goedbloed, J. P. 1983, Lecture Notes on Ideal Magnetohydrodynamics, Rijnhuizen Report, 76

Hood, A. W., Priest, E. R., & Anzer, U. 1992, Sol. Phys., 138, 331

Joarder, P. S., & Roberts, B. R. 1992, A&A, 261, 625

Joarder, P. S., Nakariakov, V., & Roberts, B. 1997, Sol. Phys., 173, 81 (JNR97)

Menzel, D. H., & Evans, J. W. 1953, Convegno Volta, 11, 119

Oliver, R., Hood, A. W., & Priest, E. R. 1996, ApJ, 461, 424

Oliver, R., & Ballester, J. L. 2001, Sol. Phys., submitted

Rempel, M., Schmitt, D., & Glatzel, W. 1999, A&A, 343, 615

Roberts, B. R., Edwin, P. M., & Benz, A. O. 1984, ApJ, 279, 857

Schmidt, G. 1979, Physics of High Temperature Plasmas (Academic Press), 128

Schmieder, B., & Mein, P. 1989 Hvar Obs. Bull. 13, IAU Colloq., 119, 31

Schmieder, B., Raadu, M., & Wiik, J. E. 1991, A&A, 252, 353

Schmitt, D., & Degenhardt, U. 1996, in Rev. Mod. Astron., ed. G. Klare (Springer-Verlag)

Simon, G., Schmieder, B., Demoulin, P., & Poland, A. I. 1986, A&A, 166, 319

Steele, C. D. C. 1996, A&A, 308, 219

Steele, C. D. C., & Priest, E. R. 1992, Sol. Phys., 140, 289

Thompson, W. T., & Schmieder, B. 1991, A&A, 243, 501

Tsubaki, T., & Takeuchi, A. 1986, Sol. Phys., 104, 313

Tsubaki, T., Ohnishi, Y., & Suematsu, Y. 1987, PASJ, 40, 121

Webb, D. F., Schmieder, B., & Rust, D. M. 1998, in New Perspectives on Solar Prominences, IAU Colloq., 167, ASP Conf. Ser., 150

Yi, Z., Engvold, O. 1991, Sol. Phys., 134, 275

Yi, Z., Engvold, O., & Keil, S. L. 1991, Sol. Phys., 132, 63